J. Fluid Mech. (1985), *vol.* 161, *pp.* 175–198
Printed in Great Britain

Numerical simulation of fully developed sinusoidal and pulsatile (physiological) flow in curved tubes

By L.-J. CHANG AND J. M. TARBELL

Department of Chemical Engineering and The Bioengineering Program, The Pennsylvania State University, 104 Fenske Laboratory, University Park, PA 16802

(Received 2 November 1984 and in revised form 4 June 1985)

Numerical solutions of the Navier–Stokes equations for fully developed, sinusoidal and pulsatile flows in curved tubes are presented for conditions not accessible to analytical perturbation methods. Simulations of physiological pulsatile flows in the aortic arch reveal a wide variety of interesting flow phenomena, including: (1) complex secondary flows with up to seven vortices in the half-tube; (2) cascaded vortex structures with vortices embedded within vortices; (3) strong secondary flows with associated wall shear stress nearly as large as the axial component; (4) reversal of axial-flow direction at the inside wall; (5) peak axial wall shear stress at the inside wall; (6) highest r.m.s. wall shear stress at the inside wall; and (7) oscillatory impedance, which is accurately described by straight-tube theory.

1. Introduction

This numerical investigation of pulsatile flow in tightly curved tubes has been undertaken for two principal reasons: (i) pulsatility and curvature may play a role in the localization of atherosclerosis ('hardening of the arteries') in certain regions of the human arterial system (Nerem & Cornhill 1980); and (ii) blood flow in the aortic arch, which is one of the most complex flows in the human circulation (Pedley 1980), is characterized by high pulsatility and curvature.

The role of fluid mechanics in the localization of atherosclerosis is not well understood at present, but the tangential stress of flowing blood on the arterial wall (wall shear stress) is believed by many to be the most likely fluid-mechanical mediator of atherosclerosis. For more than fifteen years there has been considerable controversy as to whether 'high shear stress' (Fry 1968, 1969) or 'low shear stress' (Caro, Fitz-Gerald & Schroter 1971) is more atherogenic. Recent reviews (Nerem 1981; Naumann & Schmid-Schonbein 1983) may be consulted for more information on the role of fluid mechanics in atherogenesis. In light of this background we will place particular emphasis on both the spatial and temporal distribution of wall shear stress in reporting our results.

Typical flow conditions in the aortic arch may be characterized as follows:

(1) The aspect ratio $\lambda \equiv R/a$, where R is the radius of curvature and a is the tube radius, is about 4.

(2) The Womersley parameters $\alpha = a(\omega/\nu)^{\frac{1}{2}}$, where ω is the fundamental frequency and ν is the kinematic viscosity, is usually between 10 and 20.

(3) The flow waveform is pulse-like: systole (flow on) takes $\frac{1}{3}$ to $\frac{1}{2}$ of the cycle and peak Reynolds number $Re \equiv 2Wa/\nu$, where W is the average axial velocity, ranges from 3000 to 5000; diastole (flow off) takes $\frac{2}{3}$ to $\frac{1}{2}$ of the cycle and the mean flow is nearly zero. The Dean number $Dn \equiv Re/\lambda^{\frac{1}{2}}$, which is often used to characterize

Authors	Nature	Parameter range	Method of solution
Lyne (1970)	Oscillatory – no mean flow	$\lambda \gg 1, \alpha \gg 1,$ $R_s \ll 1$ or $R_s \gg 1$	Perturbation
Zalosh & Nelson (1973)	Oscillatory – no mean flow	$\lambda \gg 1$, arbitrary α $R_s \ll 1$	Perturbation, finite Hankel transformation
Bertelson (1974)	Oscillatory – no mean flow	Arbitrary λ, $\alpha \gg 1$, $R_s \ll 1$	Perturbation
Smith (1975)	Oscillatory with mean flow	$\lambda \gg 1, \alpha \gg 1$ or $\alpha \ll 1$, $D \gg 1$ or $D \ll 1$ or $D \sim 1$, $R_s \sim 1$ or $R_s \sim D$ or $R_s \sim D^{\frac{1}{3}}$	Perturbation
Simon, Chang & Chow (1977)	Oscillatory with mean flow	$\lambda \gg 1, \alpha = 0.5 \sim 5$, small R_s $(k \sim 1)$ $Dn = 1 \sim 40$	Perturbation, finite Hankel transformation
Singh, Singha & Agarawal (1978)	Pulsatile with mean flow	Valid only for a small entrance region	Perturbation

TABLE 1. Summary of previous analytical works. $D = Ga^3/\rho\nu^2\lambda$, where G is the pressure gradient associated with the steady-flow component of the motion.

Authors	Nature	Parameter range	Method of solution
Chandran *et al.* (1974)	Oscillatory – no mean flow, elastic tube	$\lambda = 10, \alpha = 9.14,$ 6.36, 5.09, peak $Dn \sim 380$	Perturbation and numerical solution; equations linearized
Blennerhassett (1976)	Oscillatory with mean flow	$\lambda \gg 1, R_s = 30 \sim 150$	Perturbation and numerical solution; mean and unsteady part solved separately
Chandran *et al.* (1979)	Pulsatile with mean flow, elastic tube	$\lambda = 5\text{–}40, \alpha = 5.7\text{–}14.2,$ $R_s \sim O(10),$ $Dn = 98 \sim 489$	Perturbation and numerical solution; mean and unsteady part solved separately
Lin & Tarbell (1980)	Oscillatory with mean flow	$\lambda = 20, \alpha = 4\text{–}46,$ $R_s \sim O(1), k < 1$	ADI method
Rabadi *et al.* (1980)	Oscillatory with mean flow	$\lambda = 100, \alpha = 1\text{–}15,$ $R_s \sim O(0), k < 1.5$	ADI method

TABLE 2. Summary of previous numerical works

curved-tube flows, takes on (time) mean values of 300–500 and peak values of 1500–2500.

(4) The secondary Reynolds number $R_s = W_{AC}/\omega\nu\lambda$, where W_{AC} is the amplitude of the oscillatory part of the average axial velocity, is typically 4000 (Pedley 1980).

(5) The ratio of the amplitude to the mean of the pressure-gradient waveform k is about 100 (Pedley 1980).

Because of these extreme conditions, aortic-arch flows have not been successfully analysed by either analytical or numerical methods.

Tables 1 and 2 summarize the previous theoretical work on oscillatory flow in curved tubes. For a more general review of flow in curved tubes consult Berger, Talbot

& Yao (1983). Many of the analytical works were developed for purely oscillatory (zero-mean) flows, and all of them suffer from either large λ or small R_s assumptions which render them inapplicable to aortic-arch flow. The analysis by Smith (1975) appears to be the most extensive perturbation work. However, aortic-arch-flow conditions are not within the parameter ranges where perturbation solutions can be obtained (see the comparison given at the end of the paper). Among the numerical works only Lin & Tarbell (1980) and Rabadi, Simon & Chow (1980) solved the complete governing equations. However, both works were restricted to small pressure-gradient variations ($k < 1.5$) and low secondary Reynolds numbers ($R_s < 1$).

In the present work we have obtained numerical results for flow conditions characteristic of the aortic arch (λ as low as 3.8, α up to 21, $R_s \sim O(1000)$, $k \sim O(100)$. Solutions for such extreme conditions have not previously been achieved by either perturbation or numerical methods.

In the next section the mathematical problem and numerical solution technique are described, and this is followed by §3 in which the results of several numerical simulations are presented and discussed.

2. Mathematical description

2.1. *Governing equations*

The governing differential equations for fully developed, time-dependent flow of a Newtonian fluid in a rigid curved tube are given below (Rabadi *et al.* 1980) while the geometry is shown in figure 1.

Axial-momentum equation

$$\alpha^2 \frac{\partial W}{\partial \tau} + A W + B \frac{\partial W}{\partial \phi} + C \frac{\partial W}{\partial r} - \frac{\partial^2 W}{\partial r^2} - \frac{1}{r^2} \frac{\partial^2 W}{\partial \phi^2} = -\frac{1}{s} \frac{\partial P}{\partial \theta}, \tag{1}$$

Vorticity-transport equation

$$\alpha^2 \frac{\partial N}{\partial \tau} + A_N N + B \frac{\partial N}{\partial \phi} + C \frac{\partial N}{\partial r} - \frac{\partial^2 N}{\partial r^2} - \frac{1}{r^2} \frac{\partial^2 N}{\partial \phi^2} = D_W, \tag{2}$$

Stream-function equation

$$\left(\frac{1}{rs} - \frac{\sin\phi}{s^2}\right) \frac{\partial \Psi}{\partial r} + \frac{1}{s} \frac{\partial^2 \Psi}{\partial r^2} - \frac{\cos\phi}{rs^2} \frac{\partial \Psi}{\partial \phi} + \frac{1}{r^2 s} \frac{\partial^2 \Psi}{\partial \phi^2} = N, \tag{3}$$

where $$s = \lambda + r \sin\phi, \quad A = \frac{1}{s^2}\left(1 + \cos\phi \frac{\partial \Psi}{\partial r} - \frac{\sin\phi}{r} \frac{\partial \Psi}{\partial \phi}\right),$$

$$B = \frac{1}{rs}\left(\frac{\partial \Psi}{\partial r} - \cos\phi\right), \quad C = -\left(\frac{1}{r} + \frac{\sin\phi}{s} + \frac{1}{rs} \frac{\partial \Psi}{\partial \phi}\right),$$

$$A_N = \frac{1}{s^2}\left(1 - \cos\phi \frac{\partial \Psi}{\partial r} + \frac{\sin\phi}{r} \frac{\partial \Psi}{\partial \phi}\right), \quad D_W = \frac{2W}{s}\left(\cos\phi \frac{\partial W}{\partial r} - \frac{\sin\phi}{r} \frac{\partial W}{\partial \phi}\right).$$

In the above, W is the axial (θ) velocity; $\partial P/\partial \theta$ is the axial pressure gradient (independent of r, ϕ and θ in fully developed flow); N is the vorticity associated with secondary flow in the (r, ϕ)-plane; and Ψ is the stream function which characterizes the secondary flow and satisfies the continuity equation (not shown). These variables are all dimensionless as a result of scaling length with the tube radius a, velocity with ν/a, pressure with $\rho \nu^2/a^2$, and time with ω^{-1}. Dimensionless parameters appearing

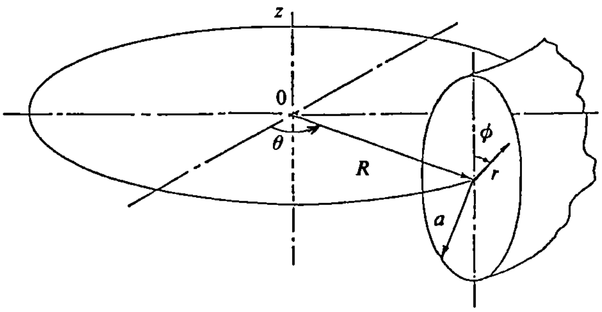

FIGURE 1. Toroidal coordinate system.

directly in the equations are the aspect ratio $\lambda \equiv R/a$, and the unsteadiness parameter $\alpha \equiv a(\omega/\nu)^{\frac{1}{2}}$. Because the flow is assumed to be fully developed, all derivatives with respect to the axial coordinate θ have been set to zero, except for the axial pressure gradient $\partial P/\partial\theta$ which drives the flow.

The boundary conditions on W, N and Ψ are derived from the no-slip condition at the tube wall ($r = 1$) and symmetry conditions about the tube centreline (W is symmetric while N and Ψ are anti-symmetric).

Boundary conditions

$$W = \Psi = 0; \quad N = \frac{1}{s}\frac{\partial^2 \Psi}{\partial r^2} \quad (r = 1, \ -\tfrac{1}{2}\pi \leqslant \phi \leqslant \tfrac{1}{2}\pi), \tag{4a}$$

$$\frac{\partial W}{\partial \phi} = \Psi = N = 0 \quad (\phi = \pm\tfrac{1}{2}\pi, \ 0 \leqslant r \leqslant 1). \tag{4b}$$

Before solving (1)–(3) subject to boundary conditions (4), the radial coordinate r is transformed (z is the new coordinate) as follows:

$$r = z\,\mathrm{e}^{k(1-z)}, \quad 0 \leqslant k \leqslant 1. \tag{5}$$

When the transformed coordinate z is discretized uniformly (Δz constant), the radial coordinate r is effectively spaced non-uniformly with close packing of nodes near the tube wall where radial gradients are steep (thin boundary layers present), and wider spacing near the tube centre where gradients are less severe. The transformed equations follow:

Axial-momentum equation

$$\alpha^2 \frac{\partial W}{\partial t} + AW + B\frac{\partial W}{\partial \phi} + (CE_1 - E_2)\frac{\partial W}{\partial z} - E_1^2 \frac{\partial^2 W}{\partial z^2} - \frac{1}{r^2}\frac{\partial^2 W}{\partial \phi^2} = -\frac{1}{s}\frac{\partial P}{\partial \theta}; \tag{6}$$

Vorticity-transport equation

$$\alpha^2 \frac{\partial N}{\partial t} + A_N N + B\frac{\partial N}{\partial \phi} + (CE_1 - E_2)\frac{\partial N}{\partial z} - E_1^2 \frac{\partial^2 N}{\partial z^2} - \frac{1}{r^2}\frac{\partial^2 N}{\partial \phi^2} = D_W; \tag{7}$$

Stream-function equation

$$\left(\frac{E_1}{rs} - \frac{\sin\phi E_1}{s^2} + \frac{E_2}{s}\right)\frac{\partial \psi}{\partial z} + \frac{E_1^2}{s}\frac{\partial^2 \psi}{\partial z^2} - \frac{\cos\phi}{rs^2}\frac{\partial \psi}{\partial \phi} + \frac{1}{r^2 s}\frac{\partial^2 \psi}{\partial \phi^2} = N; \tag{8}$$

where
$$s = \lambda + r\sin\phi, \quad A = \frac{1}{s^2}\left(1 + E_1\frac{\partial\psi}{\partial z}\cos\phi - \frac{\sin\phi}{r}\frac{\partial\psi}{\partial\phi}\right),$$
$$B = \frac{1}{rs}\left(E_1\frac{\partial\psi}{\partial z} - \cos\phi\right), \quad C = -\left(\frac{1}{r} + \frac{\sin\phi}{s} + \frac{1}{rs}\frac{\partial\psi}{\partial\phi}\right),$$
$$A_N = \frac{1}{s^2}\left(1 - E_1\frac{\partial\psi}{\partial z}\cos\phi + \frac{\sin\phi}{r}\frac{\partial\psi}{\partial\phi}\right),$$
$$D_W = 2\frac{W}{s}\left(E_1\frac{\partial W}{\partial z}\cos\phi - \frac{\sin\phi}{r}\frac{\partial W}{\partial\phi}\right),$$
$$E_1 = \frac{z}{r - krz}, \quad E_2 = -E_1^2\left(\frac{z - rE_1}{z^2} - k\right).$$

The accompanying boundary conditions are

$$W = \psi = 0; \quad N = \frac{E_1^2}{s}\frac{\partial^2\psi}{\partial z^2} \quad (z = 1, \ -\tfrac{1}{2}\pi \leqslant \phi \leqslant \tfrac{1}{2}\pi), \tag{9a}$$

$$\frac{\partial W}{\partial\phi} = \psi = N = 0 \quad (\phi = \pm\tfrac{1}{2}\pi, \ 0 \leqslant z \leqslant 1). \tag{9b}$$

2.2. *Solution procedure*

A finite-difference numerical solution was implemented on a uniformly spaced (non-staggered) 21 × 21 polar grid system. This same grid was also employed in several previous numerical works concerned with curved-tube flows (Austin & Seader 1973; Patankar, Pratap & Spalding 1974; Rabadi *et al.* 1980). The parameter k of the radial grid transformation was usually set between 0.5 and 0.7. Time increments were uniform for all simulations. Eighty-two time steps per period were employed for sinusoidal-flow simulations and 164 steps per period for pulsatile-flow simulations.

Finite-difference approximations to the partial derivatives in (6)–(8) were taken as standard second-order central differences for all spatial derivatives and first-order forward differences for time derivatives as required by the alternating-direction-implicit (ADI) algorithm. Wall vorticities (9a) were computed to first-order accuracy, and axial-wall-shear rates were calculated from a cubic-spline fit of the axial-velocity profiles. The secondary wall-shear rate was given directly by the boundary vorticity.

The time-integration scheme employed to advance the W, N and Ψ fields one time step is outlined in flow-chart fashion in figure 2. Briefly, the pressure gradient is specified and the parabolic axial-momentum equation is advanced a full time step by the ADI method without iteration. During this step, the Ψ-dependent coefficients (A, B, C) are computed from the most-current Ψ field. Next, the parabolic vorticity-transport equation is updated by the ADI method without iteration. The new coefficients (A_N, D_W) as well as the boundary vorticity (9a) are computed from the current Ψ-field and the newly computed W-field. With a new vorticity field available, the elliptic stream-function equation is advanced by the ADI method, which in this case requires iteration. A line-by-line over-relaxation method is employed for this purpose, and iteration is halted when the relative change between successive fields is less than 10^{-4} at all nodes. Having a new Ψ-field in hand, it is now possible to update the coefficients A, A_N, B and C as well as the boundary vorticity. All coefficients (A, A_N, B, C, D_W) are evaluated at the central grid point.

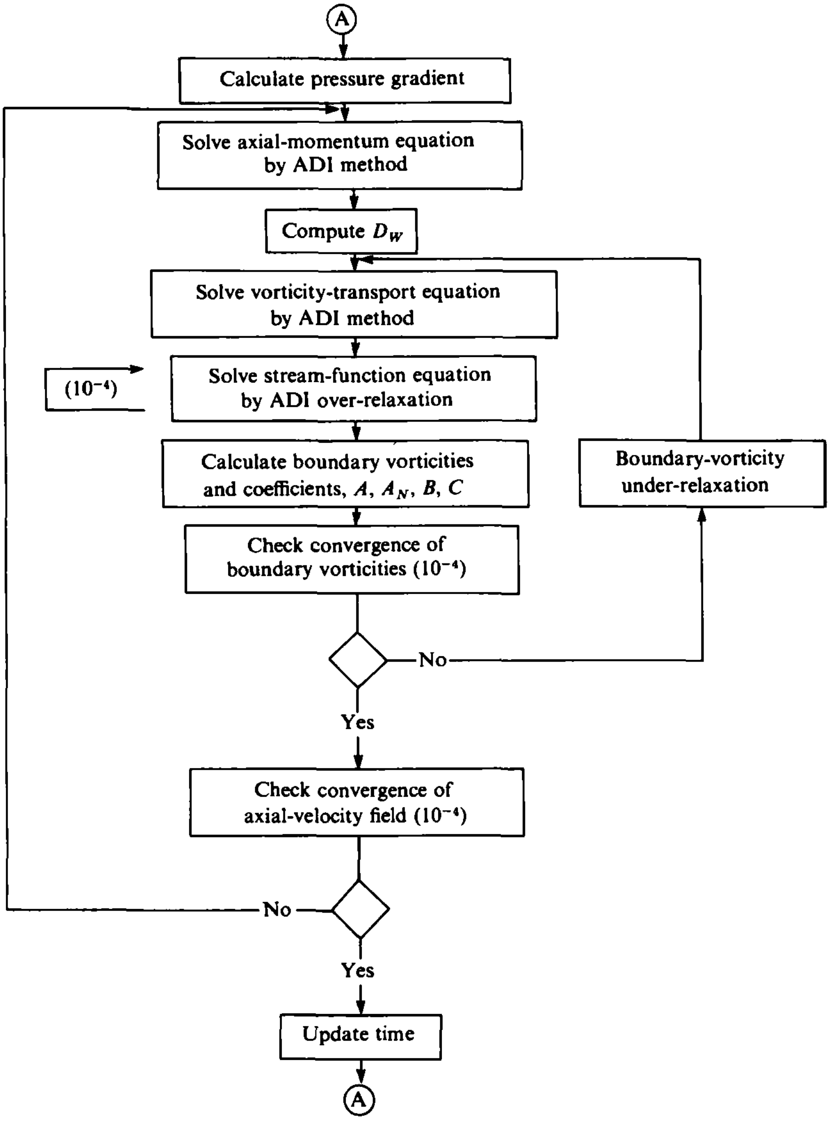

FIGURE 2. Flow chart for numerical algorithm.

Experience has shown that it is important, for purposes of maintaining numerical stability, to obtain convergence of both the vorticity-transport and stream-function equations before proceeding with another iteration of the axial-momentum equation. The stability of this iteration loop is maintained through under-relaxation (typical relaxation factor is 0.5) on the boundary-vorticity values. Once this stream function–vorticity loop has converged (less than 10^{-4} relative change) the outer iteration loop for the axial velocity can be continued until convergence (again, less than 10^{-4} relative change) is achieved. This sequence of three nested iteration loops is then repeated at each successive time step. Integration is continued over several periods of pulsatile flow until an oscillatory steady state is obtained.

Initial conditions for the algorithm in the case of pulsatile flow were provided in a very simple manner. The flow was assumed to be stationary ($W = N = \Psi = 0$) throughout the tube cross-section at the end of diastole just prior to the rapid systolic acceleration. This initial condition allowed an oscillatory steady state to be approached within 4–10 periods for all cases to be presented.

Although grid-refinement studies of numerical convergence were not pursued because of excessive computation time, the numerical method was extensively checked against previous numerical work and perturbation solutions. A comparison with the axial-velocity profiles of steady flow with $Dn = 401.3$ and $\lambda = 5.0$ simulated by Austin & Seader (1973) showed a maximum relative discrepancy of less than 1 %. Two cases of purely oscillatory flow, one with $\alpha = 21.92$, $\lambda = 9.256$, $R_s = 1.09$, which is an experimental condition of Bertelson (1974), and another with $\alpha = 17$, $\lambda = 20$, $R_s = 500$, showed Lyne's four-vortex secondary flow and steady secondary streaming phenomena (Lyne 1970). The time-averaged secondary velocities, when compared with perturbation solutions, showed a maximum relative difference of less than 4 %, which may well be attributed to the approximate nature of the perturbation solutions.

3. Results and discussion

We have simulated two sinusoidal flows with non-zero mean and two physiological pulsatile flows characteristic of the aortic arch. All of the simulations are based on experiments conducted in physical models by others in which extensive axial and limited secondary-velocity data were measured by either laser-Doppler or hot-film anemometry. We have attempted to compare quantitatively our simulations with the experiments where feasible, particularly the axial-velocity profiles. The secondary-flow structure revealed by the simulations is much more complex than suggested by the experimental results.

3.1. *Sinusoidal flow with non-zero mean*

Talbot & Gong (1983) conducted two experiments (hereinafter referred to as Exp. I and Exp. II) in curved tubes by generating sinusoidal flows superimposed on a mean flow. Four observation sections were set up along the axial path of the developing flow, and a laser-Doppler anemometer was employed to measure axial and radial velocities. Since our simulations are strictly applicable to fully developed flows, only the experimental results for the last sections ($\theta = 135°$ in Exp. I and $\theta = 110°$ in Exp. II) will be used for comparison.

A major problem encountered in simulating these experiments is the unavailability of the pressure-gradient waveform, which is the forcing function for the governing differential equations. This function is seldom reported in the experimental literature – usually only the flow waveforms are available. However, the experiments of Kang & Tarbell (1983) led to a simple theory relating pressure gradient and flow in curved-tube sinusoidal flows with a mean component. The theory indicates that the impedance (pressure drop/flow rate) of the mean-flow and the oscillatory-flow components are additive; the oscillatory part is the same as that of fully developed flow in a rigid straight tube (Womersley 1955); and the mean part is described by a quasi-steady-state analysis based on a correlation for the steady-flow impedance of curved tubes due to Tarbell & Samuels (1973). The details are available in Kang

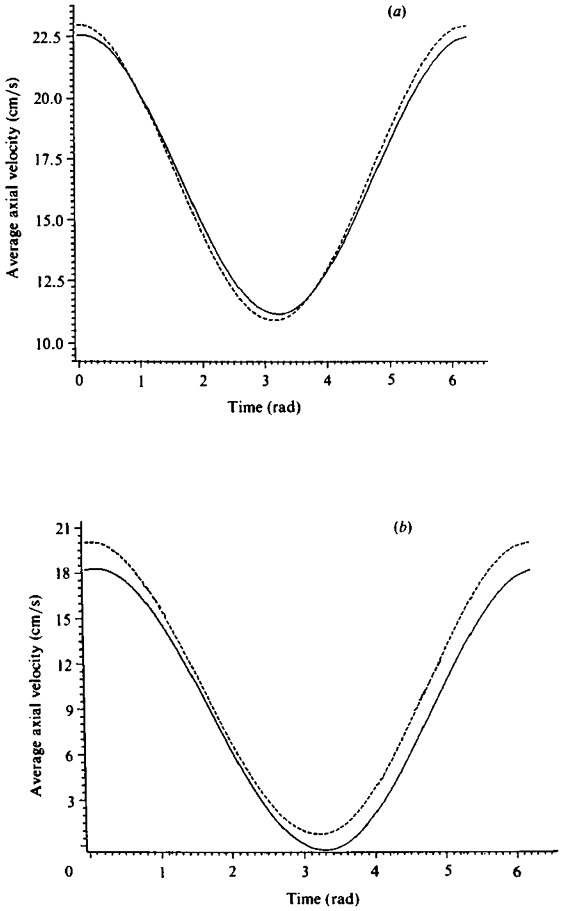

FIGURE 3. Flow waveforms for Exp. I (*a*) and Exp. II (*b*). —, experiment; ---, simulation.

& Tarbell (1983). When this theory was applied to the flow waveforms reported by Talbot & Gong (1983), the pressure gradients below were obtained:

$$\text{Exp. I} \quad \frac{\partial P}{\partial \theta} = 69737[1+1.98\cos(\omega t+1.32)];$$

$$\text{Exp. II} \quad \frac{\partial P}{\partial \theta} = 94414[1+6.54\cos(\omega t+1.32)].$$

These waveforms have been employed as inputs for simulation of Exp. I and Exp. II. The experimental and simulated-flow waveforms are shown in figure 3. Values of relevant parameters are summarized in table 3.

As pointed out by Talbot & Gong (1983), Exp. I is essentially in a quasi-steady state. The oscillatory part of the pressure gradient merely modulates the basic steady flow. This is also observed in the numerical results. Figure 4 shows axial-velocity contours (lines of constant axial velocity) and secondary-flow-velocity vectors (length proportional to velocity) at two times during a cycle for Exp. I. Axial velocities are always highest near the outer wall, and the secondary flow always consists of a single vortex (in the half tube) with flow directed outward along the centreline. These are the qualitative features of steady flow in a curved tube first reported by Dean (1927).

	Dn	Peak *Dn*	λ	α	R_s	*k*
Exp. I	120	163	20	7	6.36	1.98
Exp. II	372	825	7	12.5	231.5	6.54

TABLE 3. Flow and pressure-gradient characteristics of Exp. I and Exp. II

Much more complex flow was observed in Exp. II. Although the numerical and experimental results show essentially the same phenomena, the former, giving both components of the secondary velocity and more nodes in the semicircle, perhaps shows the qualitative features of the secondary flow more clearly. The axial velocity contours and secondary flows are shown in figures 5(*a*)–(*f*) and 6(*a*)–(*f*) which correspond to figures 7(*a*)–(*f*) ($\theta = 110°$) in Talbot & Gong (1983).

The numerical axial-velocity contours are both qualitatively and quantitatively comparable to the experimental contours. The maximum axial velocity still occurs on the outside wall, but the profile at peak forward flow (figure 5*a*) is much flatter than in Exp. I (cf. figure 4*a*). In Exp. II there is significant axial-flow reversal along the inside wall over a substantial portion of the cycle (figure 5*c*, *d*) even though the mean flow shows no reversal (figure 3). This flow reversal has no counterpart in fully developed steady flow, but may arise in oscillatory flows at high α even in straight tubes (Womersley 1955).

The secondary-flow phenomena of Exp. II are displayed in figure 6 both quantitatively (velocity vectors on left) and qualitatively (streamline sketches on right). The streamline sketches simply depict the major vortex structures without attempting to convey the tortuosity of individual streamlines. Weak vortices that, in a few instances, seem to be required for topological consistency but are difficult to resolve with our finite-difference grid have not been included. In figure 6(*a*), the secondary flow shows a single vortex (Dean vortex) with its centre near the inside wall and many complex streamlines. High velocities appear along the wall, particularly near the inside of the tube. Talbot & Gong (1983) described this high-velocity flow near the inside wall as a 'jet-like outward motion'. Subsequent deceleration of the flow results in the formation of an embedded vortex (within the Dean vortex) near the inner wall (figure 6*b*). This corresponds to what Talbot & Gong (1983) described as 'imbedded secondary flow helical motion'. The Dean vortex is confined to the upper part of the half-tube and tends to drive a weak clockwise inner vortex. The experimental data also showed evidence of this weak vortex since small inward velocities between the outer wall and the centre of the tube were observed. In figures 6(*c*)–(*e*), the embedded vortex continues to exist but the weak clockwise vortex of figure 6(*b*) has disappeared. Figure 6(*f*) again shows this embedded vortex, but a companion vortex of considerable momentum is now also observed. These two strong vortices probably underlie the 'four distinct regions of secondary motion, two outward and two inward' which were described by Talbot & Gong (1983) for this instant in the flow cycle. The Dean vortex in this case has tortuous streamlines near the outside wall (cf. figure 6*a*) where there is a hint of flow separation accompanied by a weak clockwise vortex. It appears that the fluid near the inside wall, which has been trapped inside the strong embedded vortex throughout most of the cycle (6*b*–*f*), has finally gained enough momentum to move to the outer wall along the centreline, and the two strong vortices observed in (6*f*) merge to form part of the single Dean vortex (6*a*).

The maximum secondary wall shear stress over the cycle is 3.68 dynes/cm^2 which

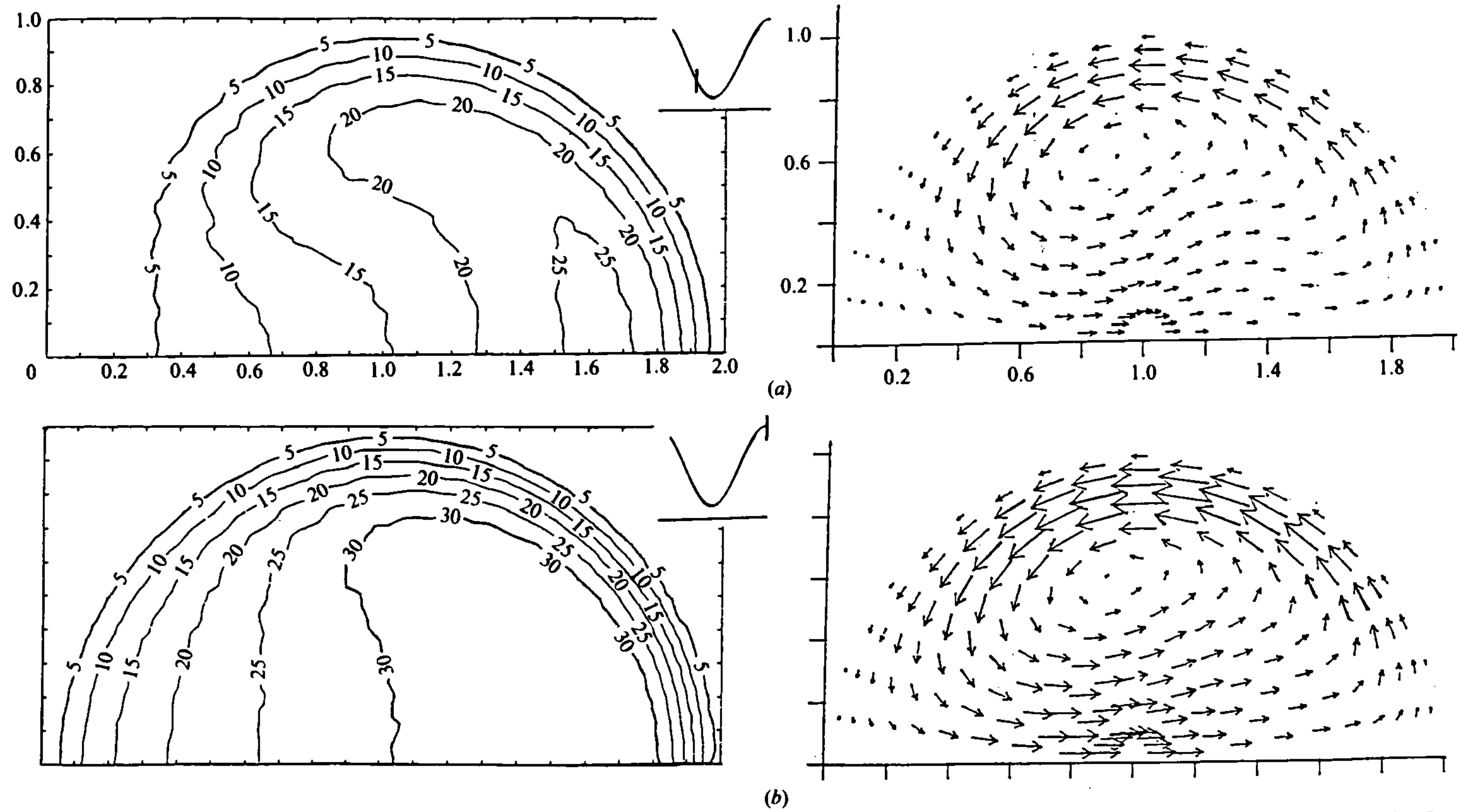

FIGURE 4. Axial-velocity contours (left) and secondary velocity vectors for Exp. I: (*a*) $t = \frac{2}{3}\pi$; (*b*) 2π. Velocity contours are in cm/s. One tube diameter length is equal to 42 cm/s for velocity vectors. Insert shows time with respect to average velocity waveform.

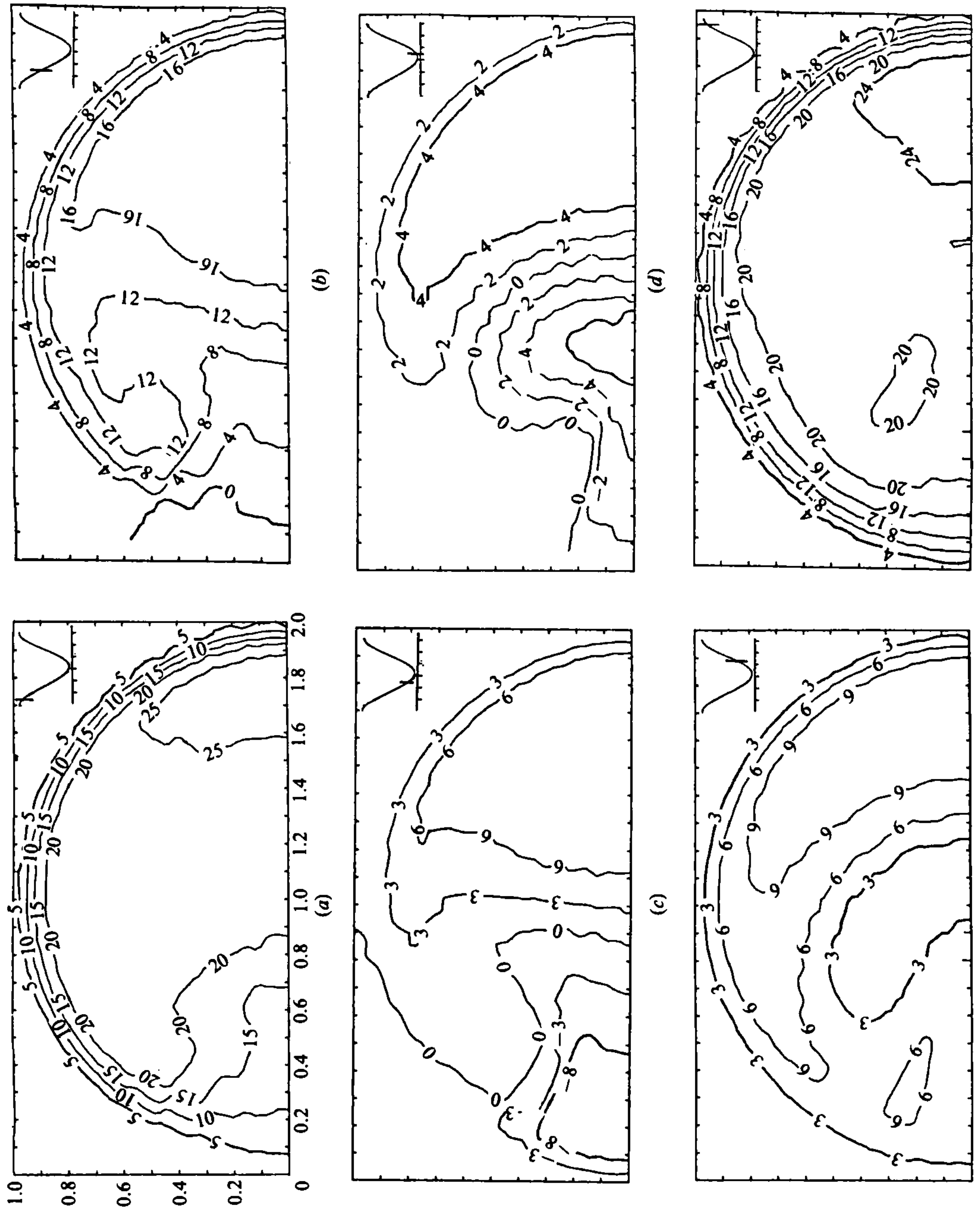

FIGURE 5. Axial velocity contours of Exp. II: (a) $t = \frac{1}{8}\pi$, (b) $\frac{3}{8}\pi$, (c) $\frac{5}{8}\pi$, (d) $\frac{7}{8}\pi$, (e) $\frac{8.5}{8}\pi$, (f) $\frac{11}{8}\pi$.

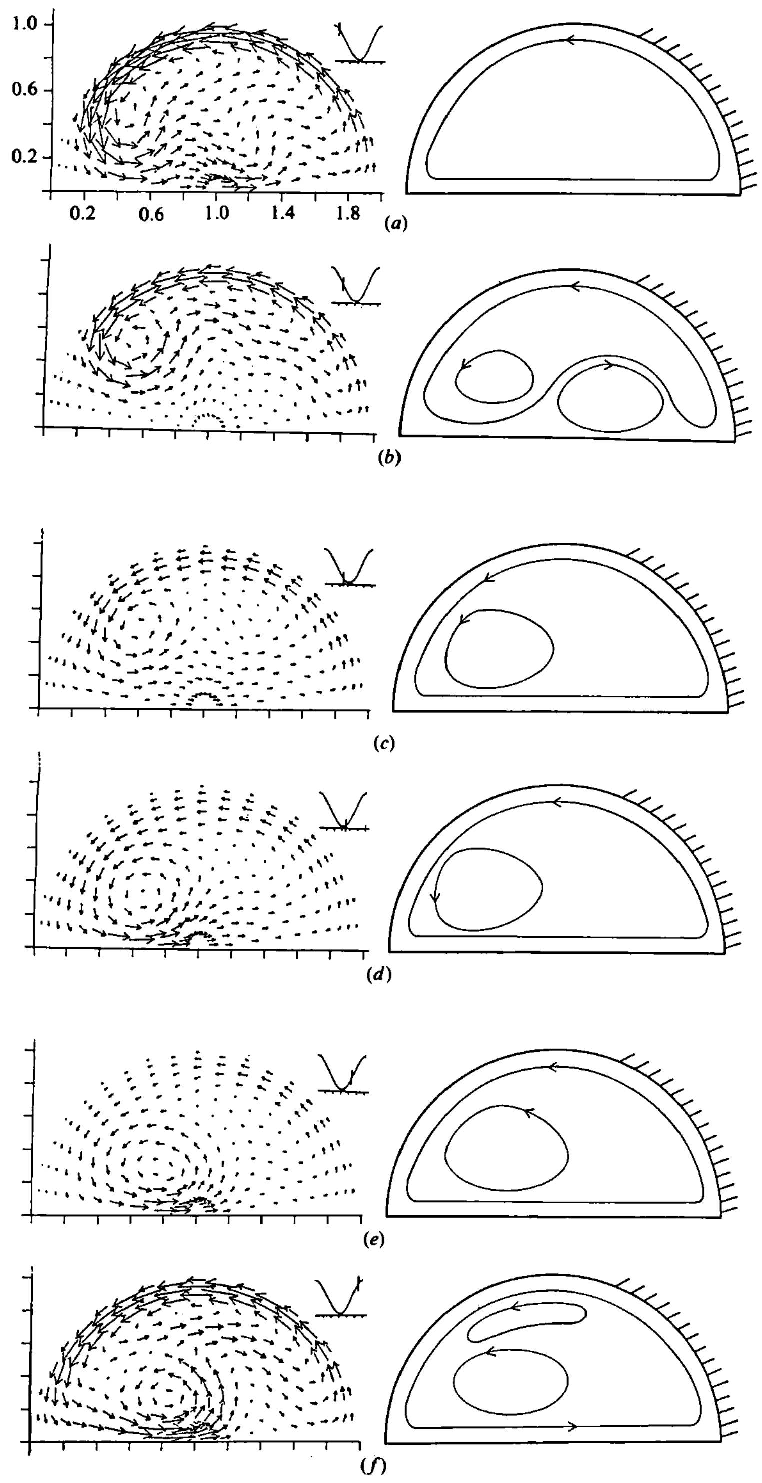

FIGURE 6. Secondary velocity vectors (left) and streamline sketches (right) for Exp. II: (*a*) $t = \frac{1}{6}\pi$, (*b*) $\frac{3}{6}\pi$, (*c*) $\frac{5}{6}\pi$, (*d*) $\frac{7}{6}\pi$, (*e*) $\frac{8.5}{6}\pi$, (*f*) $\frac{11}{6}\pi$. One tube diameter length is equal to 36.8 cm/s.

occurs at the top of tube ($\phi = 0°$) at time $\frac{1}{8}\pi$. The axial wall shear stress reaches its maximum value of 6.14 dynes/cm^2 at time 0.153 at the outside of the tube ($\phi = 90°$). These values should be compared with a peak Poiseuille-flow wall shear stress of 1.34 dynes/cm^2 and a peak Womersley-flow wall shear stress of 4.18 dynes/cm^2.

3.2. *Physiological pulsatile flows*

In this section we discuss simulations of two physiological pulsatile flows that are related to recent experiments in which velocity fields were measured. The experiment of Chandran & Yearwood (1981) (hereinafter referred to as Exp. III) was performed in an acrylic curved tube of constant radius of curvature and circular cross-section with an aspect ratio of $\lambda = 10$. The experiment of Yearwood & Chandran (1984) (hereinafter referred to as Exp. IV) was conducted in a rigid model produced from a silicone-rubber casting of a human aortic arch, excluding the branches at the top of the arch. The radius of the aortic-arch model tapered from 1.63 cm in the ascending aorta to 1.15 cm in the descending aorta. Since our simulation dealt only with fully developed flow, an average radius of 1.35 cm and an average aspect ratio of $\lambda = 3.8$ were used. Thus, we roughly approximated the geometry of Exp. IV.

In both experiments a three-component hot-film probe was employed to measure axial and secondary velocities at five axial locations starting at the entrance. The last observation section, where comparisons with simulations will be made, was at 97° from the entrance for Exp. III and 186.2° for Exp. IV. The simple theory described in §3.1 was used to provide an estimate of the unknown pressure gradient from the flow waveforms reported for Exps. III and IV, and some adjustments were necessary to obtain the desired flow waveforms. The pressure-gradient waveforms are shown in figure 7 and the flow waveforms in figure 8. Values of important parameters are summarized in table 4.

Axial-flow phenomena. Figures 9 and 10 show both simulated and measured axial-velocity profiles at the central line ($\phi = -\frac{1}{2}\pi$ to $+\frac{1}{2}\pi$) and the top-centreline ($\phi = 0$) for Exp. III. The agreement between simulation and experiment is quite good, even though the flow waveforms do not match exactly. The profiles show that velocities near the inner wall go through a larger cyclic variation than those near the outer wall, and significant reverse flows are observed near the inner wall during diastole. The simulation results show that the maximum axial velocity occurs near the outer wall at time 4.90, while the maximum axial wall shear stress appears at the inside wall at time 3.76. The top-centre profiles are relatively flat and do not show reversal.

The simulated distribution of the axial wall shear stress around the periphery is displayed in figure 11, while the peak, mean and r.m.s. values at three locations are summarized in table 5. The peak wall shear stresses at the inner and outer wall are very close, with the inner wall having a slightly higher value of 22.7 dynes/cm^2. The approximate peak wall shear stresses reported by Chandran & Yearwood (1981) are 11.5 dynes/cm^2 for the outer wall and 10 dynes/cm^2 for the inner wall. The discrepancies between simulation and experiment may in part reflect the errors involved in calculating wall shear stresses from extrapolated velocity-profile measurements in the near-wall region. As pointed out by Brech & Bellhouse (1973), this method may underestimate the real values by 50%. For comparison, the peak Poiseuille-flow wall-shear-stress value is 5.1 dynes/cm^2 while the peak forward-Womersley-flow wall shear stress is 21.0 dynes/cm^2. Womersley flow for this experimental condition also shows reversal of wall-shear-stress direction with a peak negative value of -10.8 dynes/cm^2. The wall shear stress reverses direction at the inside wall, but not the outside wall, and the cyclic variation is greater at the inside

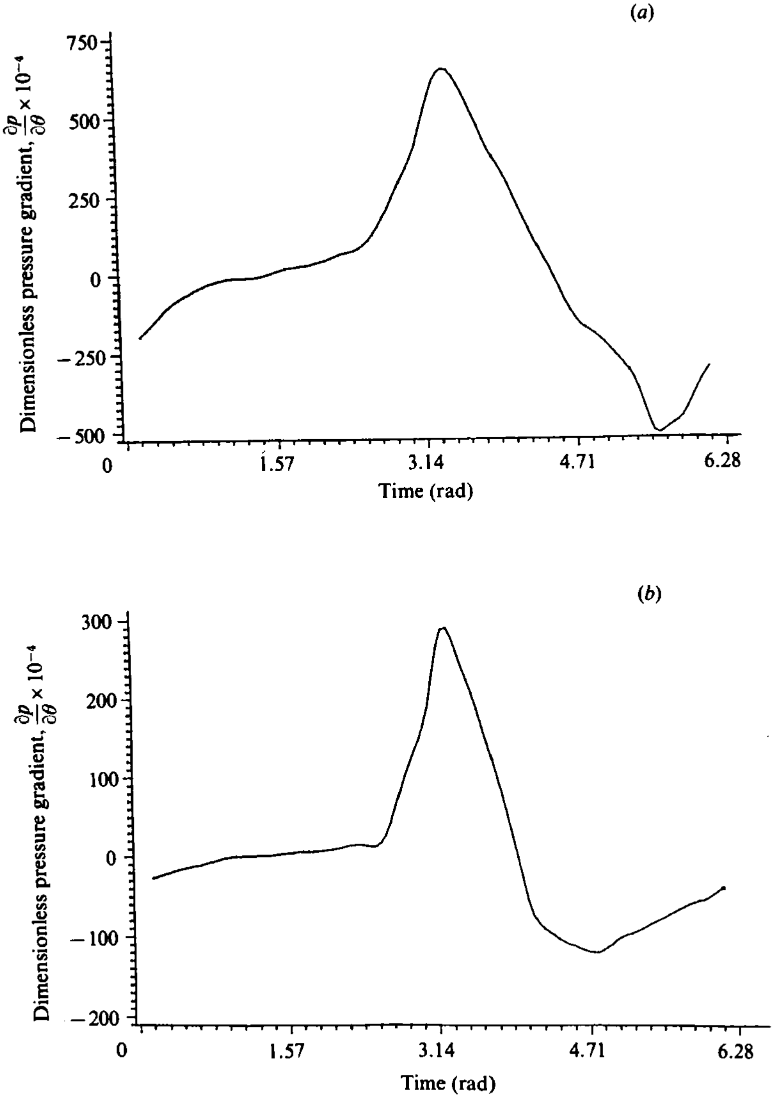

FIGURE 7. Pressure gradient waveforms: (*a*) Exp. III; (*b*) Exp. IV.

wall. This is reflected in the higher r.m.s. values at the inside wall (table 5). However, the (time) mean value is considerably higher at the outside wall, as would be expected in steady flow.

The axial-flow phenomena of Exp. IV are similar to those of Exp. III. Figures 12–14 show the simulated central-line axial-velocity profiles, top-centre axial-velocity profiles, and the axial-wall-shear-stress distributions, respectively. Peak, mean and r.m.s. values of axial wall shear stress at three locations are also presented in table 5. The quantitative comparison between simulation and experiment is not as favourable in this case as it was for Exp. III; however, the geometry in Exp. IV can only be roughly approximated as a uniform curved tube. Nonetheless, the comparisons are fairly good. Near the peak of systole the fluid near the inner wall displays a significantly higher velocity than that near the outer wall. The experimental profile

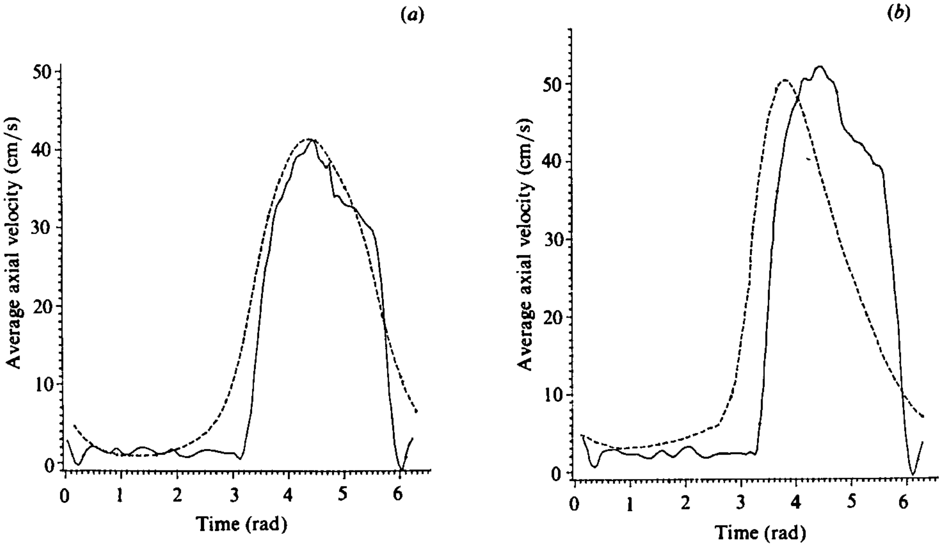

FIGURE 8. Flow waveforms: (*a*) Exp. III; (*b*) Exp. IV. —, experiment; ---, simulation.

	Dn	Peak *Dn*	λ	α	R_s	*k*
Exp. III	380	987	10	20.76	215.7	52.1
Exp. IV	594	1740	3.8	18.58	950.8	48.0

TABLE 4. Flow and pressure-gradient characteristics of Exp. III and Exp. IV

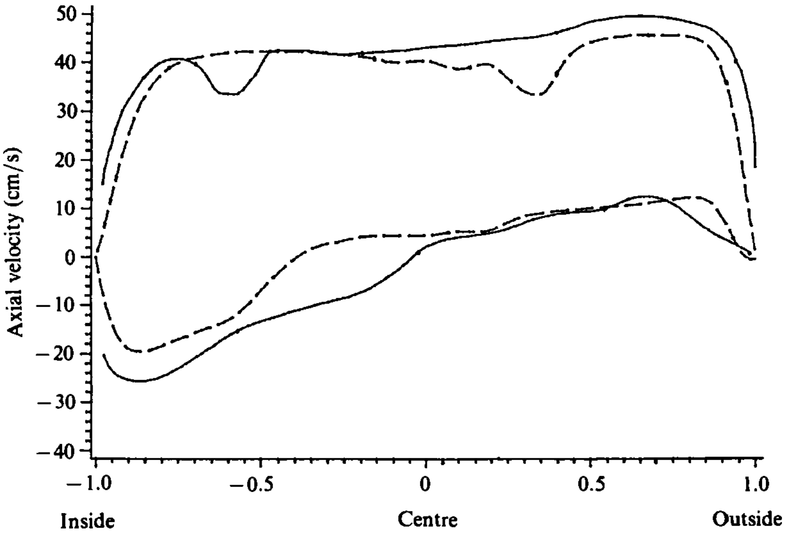

FIGURE 9. Central-line axial-velocity profiles for Exp. III. —, experiment; ---, simulation: $t = 4.90$ or $J = 6$ in Chandran & Yearwood (1981) for upper two profiles; $t = 0.31$ or $J = 10$ in Chandran & Yearwood (1981) for lower two profiles.

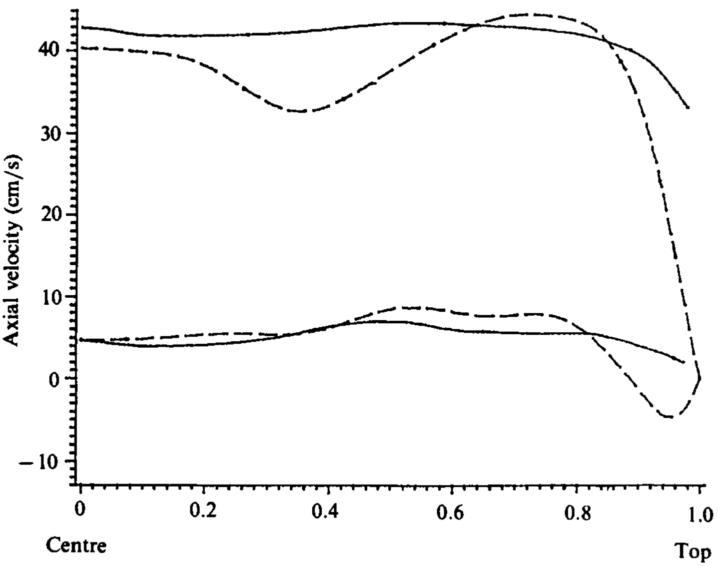

FIGURE 10. Top-centreline axial-velocity profiles for Exp. III. —, experiment; ---, simulation: $t = 4.90$ or $J = 6$ in Chandran & Yearwood (1981) for upper two profiles; $t = 0.31$ or $J = 10$ in Chandran & Yearwood (1981) for lower two profiles.

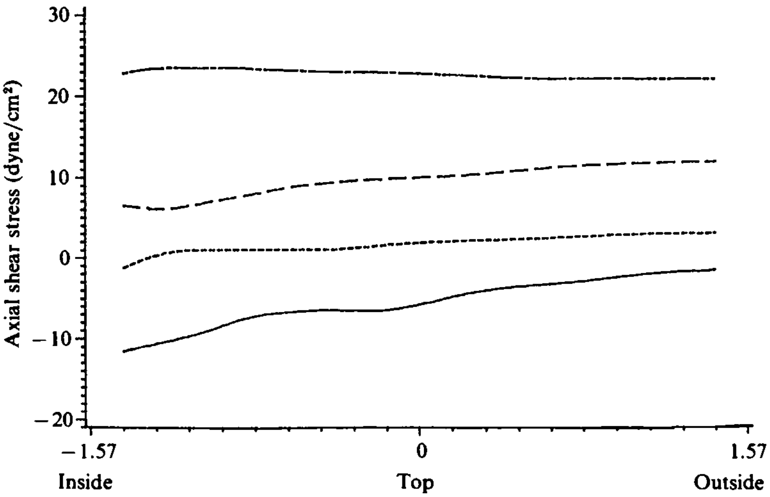

FIGURE 11. Simulated axial wall shear stress distributions for Exp. III.
—, $t = 0.31$; ---, 2.30; ----, 3.75; ---, 4.90.

	Inside			Top			Outside		
	peak	mean	r.m.s.	peak	mean	r.m.s.	peak	mean	r.m.s.
Exp. III	22.69	1.14	11.84	22.73	4.99	10.79	22.05	6.79	10.67
Exp. IV	38.79	0.71	15.72	32.40	7.10	12.67	27.50	9.20	11.99

TABLE 5. Axial-wall-shear-stress characteristics. All values in dynes/cm².

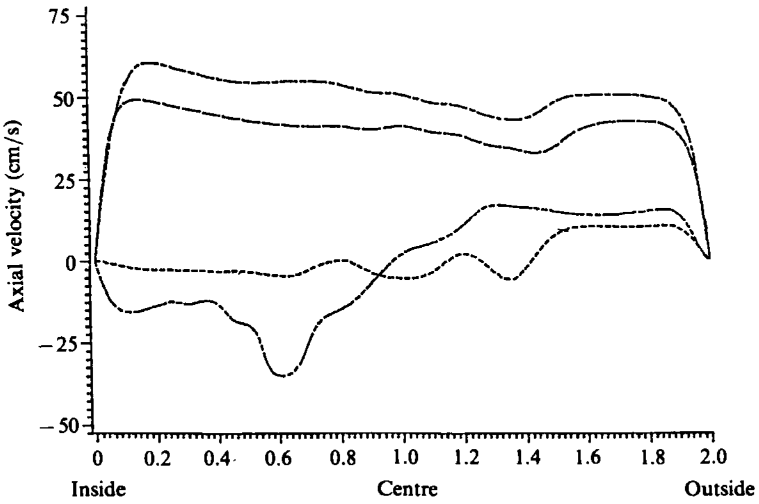

FIGURE 12. Central-line axial-velocity profiles for Exp. IV. ---, $t = 2.15$; ———, $t = 3.52$; ----, $t = 3.83$; ----, $t = 6.28$.

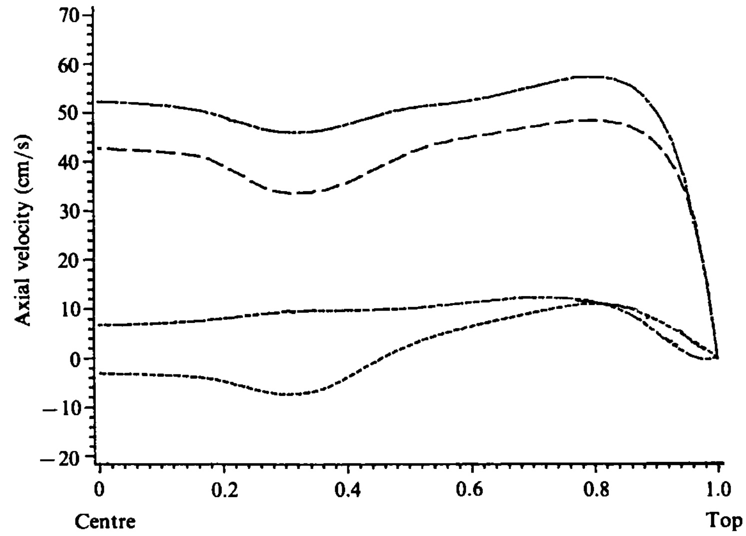

FIGURE 13. Top-centreline axial-velocity profiles for Exp. IV. ---, $t = 2.15$; ———, 3.52; ----, 3.83; ----, 6.28.

also shows this feature. As in Exp. III, velocities near the inner wall go through larger cyclic variations than those near the outer wall, and significant reverse flows are observed near the inner wall. This was also observed experimentally. The top-centre profiles are relatively flat, as in Exp. III, but there is now evidence of flow reversal during diastole.

Again, the axial wall shear stress displays the largest r.m.s. values and lowest mean values, as well as significant negative values at the inner wall – not the outer wall. However, unlike the situation in Exp. III, the maximum axial wall shear stress is significantly higher at the inside wall (38.8 dynes/cm^2) than it is at the outside wall

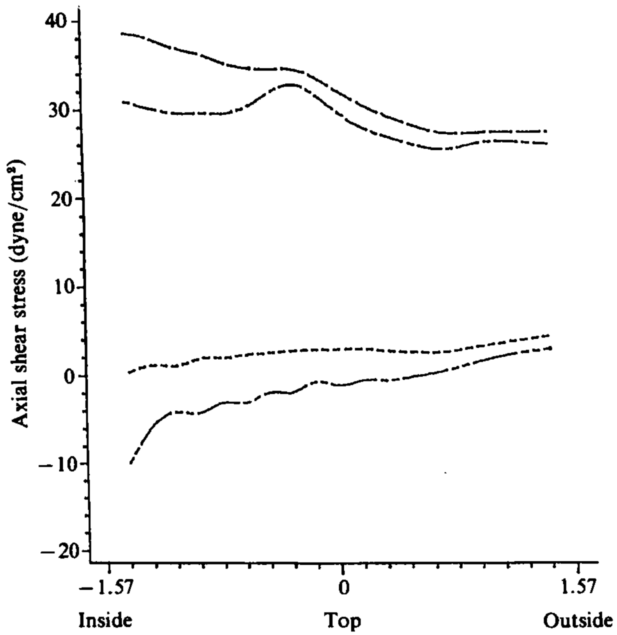

FIGURE 14. Simulated axial-wall-shear-stress distributions for Exp. IV. ---, $t = 2.15$; ——, 3.52; ----, 3.83; ---–, 6.28.

(26.0 dynes/cm^2). The reported data by Yearwood & Chandran (1984) show a similar trend, but the values are lower, with 18.5 dynes/cm^2 at the inner wall and 14.0 dynes/cm^2 at the outer wall. For comparison, the peak Poiseuille-flow wall shear stress value is 7.0 dynes/cm^2 while, for Womersley flow, the peak forward-flow wall shear stress is 25.0 dynes/cm^2 and the peak negative-flow value is -6.4 dynes/cm^2.

The impedance (pressure drop/flow rate) of the first seven harmonics of the simulated flows is displayed in figure 15. The impedance modulus has been normalized in such a way that a value of 1 is obtained for Poiseuille flow. It is striking to note how well the impedance of pulsatile flow in tightly curved tubes is described by straight-tube theory (Womersley 1955). This is exactly what was observed by Kang & Tarbell (1983) in flow-pressure-drop experiments in a variety of curved-tube models for sinusoidal flows with non-zero mean. Apparently, in the wall region (Stokes layer) at high α, the axial component of the inertia ($\partial V/\partial t + V \cdot \nabla V$ in the Navier–Stokes equations) is dominated by the unsteady term ($\partial V/\partial t$). The unsteady inertia is linear, geometry independent and, of course, accounted for in straight-tube theory. In fact, high-α-perturbation solutions for oscillatory flow in curved tubes by Lyne (1970) (pure sinusoidal flow with zero mean flow) and Blennerhassett (1976) (sinusoidal flow with a non-zero mean when the Stokes layer is the thinnest boundary layer) produce the straight-tube result at the leading order.

The impedance of the mean flow was determined to be 2.57 in Exp. III and 3.37 in Exp. IV. For steady flow at the mean Dean number of the pulsatile flow simulations, the impedances may be estimated by the correlation of Tarbell & Samuels (1973). This correlation accurately predicts both experimental (Kang & Tarbell 1983) and numerical (Tarbell & Samuels 1973) results in ranges of aspect ratio and Dean number appropriate to the present study. The resulting steady-flow impedances are 2.65 for Exp. III and 4.10 for Exp. IV. In both cases the mean

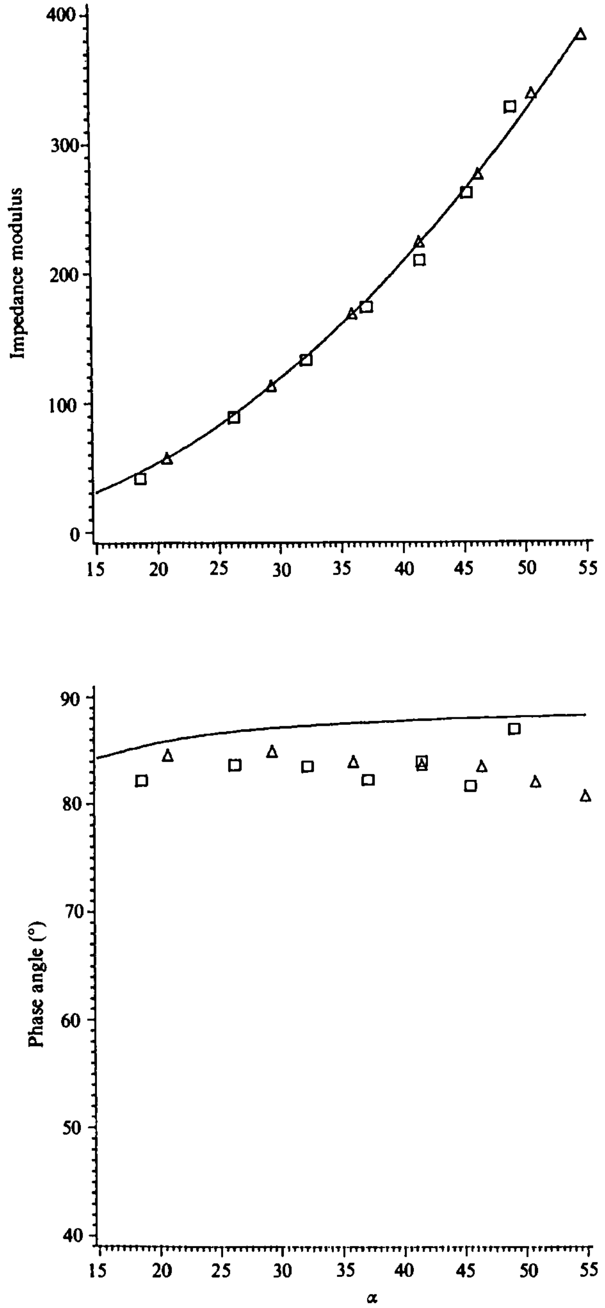

FIGURE 15. Impedance modulus and phase angle for Exp. III and IV. △, Exp. III; □, Exp. IV; —, straight-tube theory.

impedance of pulsatile flow is lower than the impedance of steady flow at the mean Dean number. This finding is in marked contrast with the experimental results of Kang & Tarbell (1983). They found that mean impedance in oscillatory flow was always higher than steady-flow impedance at the mean Dean number. However, Kang & Tarbell (1983) considered only sinusoidal flows with unsteadiness-parameter values in the range $\alpha = 4$–17, whereas Exps. III and IV simulated in this work involved pulsatile flows with unsteadiness parameters in the range $\alpha = 18$–55 (when seven harmonics are considered). It should be noted that for the simulations of Exps. I and II, which involve flow conditions similar to the experiments of Kang & Tarbell (1983), the mean-flow impedance is always greater than the steady-flow impedance at the mean Dean number – by a factor of 1.01 for Exp. I and 1.09 for Exp. II. Thus, differences in flow waveform and/or unsteadiness-parameter range seem to be important in explaining the difference in mean-flow behaviour, but the mechanism(s) operative are not clear at the present time.

Secondary-flow phenomena. The discussion of qualitative secondary-flow phenomena is confined to Exp. IV, which simulates physiological-pulsatile-flow conditions in the human aortic arch. For Exp. III the qualitative features are very similar to those of Exp. II. Secondary-flow velocity vectors and streamlines at four instants during the cardiac cycle are displayed in figure 16. The secondary-flow pattern at end diastole is shown in figure 16*a*. There appear to be three vortices, one clockwise and two counterclockwise, embedded within a large counterclockwise vortex (Dean vortex). This pattern of embedded vortices is qualitatively similar to patterns observed in Exp. II (figure 6*c*–*e*), although more vortices are embedded here. The behaviour at peak systole (figure 16*b*) is qualitatively different. Here the Dean vortex is confined to the wall region and the core flow is composed of three counter-rotating vortices – two clockwise and one counterclockwise. This pattern is similar to that originally predicted by Lyne (1970) for pure sinusoidal flow at high α, but the core flow is more complex here. By late systole (figure 16*c*) the Dean vortex appears to have pushed its way into the core, engulfing vortices in the process. This continues until at end systole (figure 16*d*), the most complex structure arises. Here we see what appears to be a single Dean vortex containing three counter-rotating vortices, but the vortex nearest the inside wall contains within it a sub-system of three counter-rotating vortices. Thus at this instant we see vortex within vortex within vortex – a structure reminiscent of turbulence of a rather coarse grain, yet there is no random time variation apparent since the instantaneous velocity values are repeated each period to within a relative variation of 10^{-4}.

The secondary-flow wall-shear-stress distributions at four instants during the cardiac cycle are reported in figure 17 (Exp. III) and figure 18 (Exp. IV). In both cases the wall shear stress peaks near the top of the tube, towards the inside wall, and there is no evidence of reversal of wall-shear-stress direction over the cycle. The secondary-flow wall shear stresses are quite large, with peak values reaching 37% of peak axial-wall-shear-stress values in Exp. III and 72% in Exp. IV.

Comparison with Smith (1975). Smith (1975), employing perturbation methods, examined the character of various fluid motions that might occur in fully developed sinusoidal flow in a rigid curved tube. He identified ten separate flow regimes depending on the values of three parameters: the alternative Dean number D, the secondary Reynolds number R_s and the frequency parameter $\beta = (2/\alpha)^{\frac{1}{2}}$. The alternative Dean number is defined as $D = Ga^3/\lambda^{\frac{1}{2}}\rho\nu^2$ where G is the pressure gradient associated with the mean-flow component of the motion.

Although Smith's analysis invokes the assumption of large λ, it is still of interest to see how the physiological pulsatile flows might be classified. We have determined from our simulations that:

$$D = 3899, \quad R_s = 215, \quad \beta = 0.068, \quad \text{for Exp. III;}$$

and

$$D = 10823, \quad R_s = 951, \quad \beta = 0.070, \quad \text{for Exp. IV.}$$

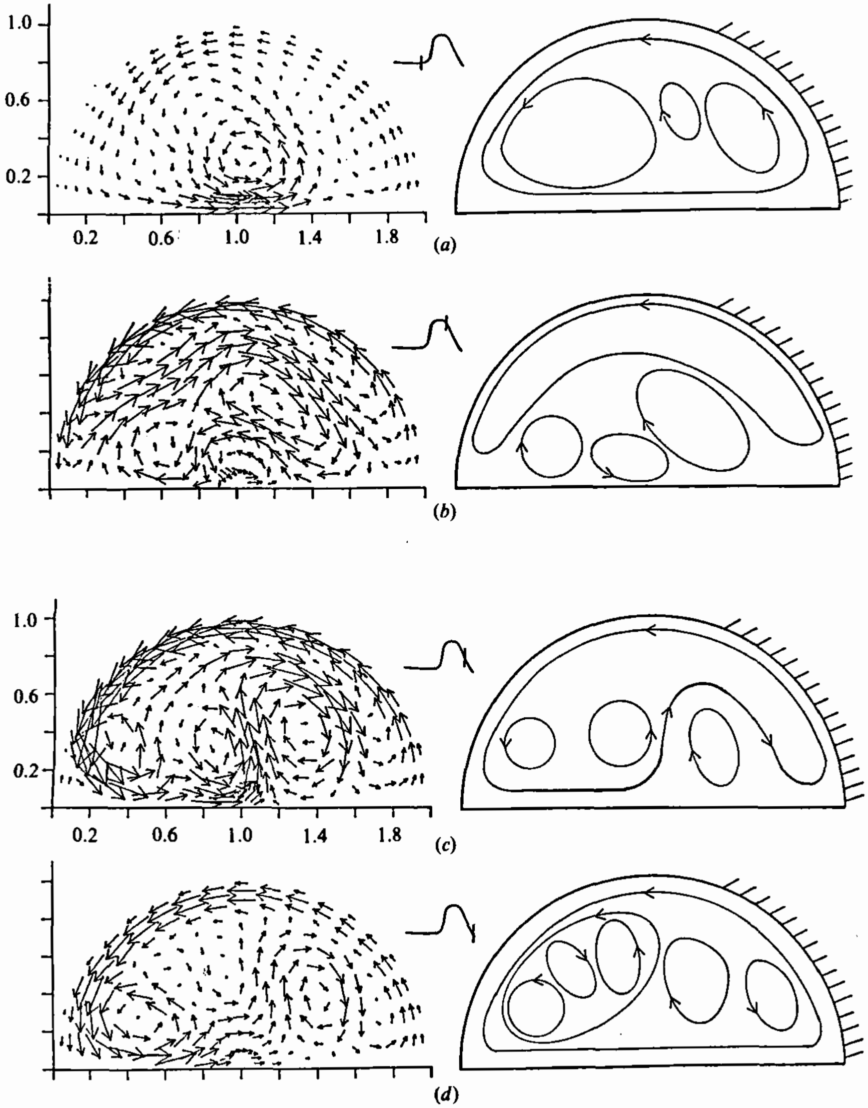

FIGURE 16. Secondary-velocity vectors (left) and streamline sketches (right) for Exp. IV: (*a*) $t = 2.15$, (*b*) 3.83, (*c*) 5.06, (*d*) 6.28, one tube diameter length is equal to 160 cm/s.

Both cases most closely correspond to Smith's case X ($D \gg 1$, $\beta \sim D^{-\frac{1}{3}}$, $R_s \sim D^{\frac{2}{3}}$). Talbot & Gong (1983) pointed out that Exp. II also corresponds to case X whereas Exp. I is closer to case V. However, for case X Smith (1975) obtains a solution form only with the further restriction $l \gg 1$ or $l \ll 1$, where $l = \beta D^{\frac{1}{3}}$. For Exps. III and IV, $l = 1.07$ and 1.68, respectively. Thus we see that the physiological pulsatile flows are outside the reach of Smith's perturbation solutions and full numerical solutions, such as ours, are in order.

It may be of interest to consider to what extent the qualitative features of Smith's Case X are manifested in the simulations of Exp. IV. For Case X, both the axial and secondary flow are pulsatile, and for $l \ll 1$ the secondary flow is definitely outward but may be reversed for $l \gg 1$. The results of Exp. IV simulations certainly show both

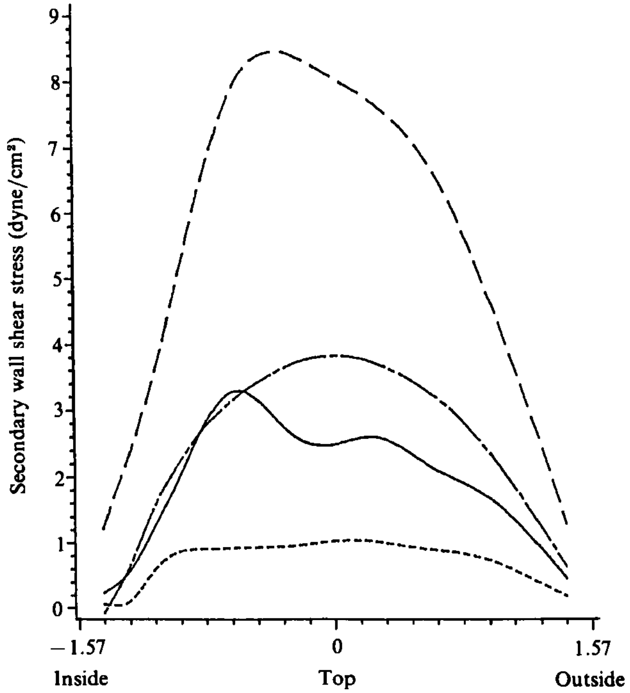

FIGURE 17. Secondary-wall-shear-stress distributions for Exp. III.
—, $t = 0.31$; ---, 2.30; –––, 3.75; –––, 4.90.

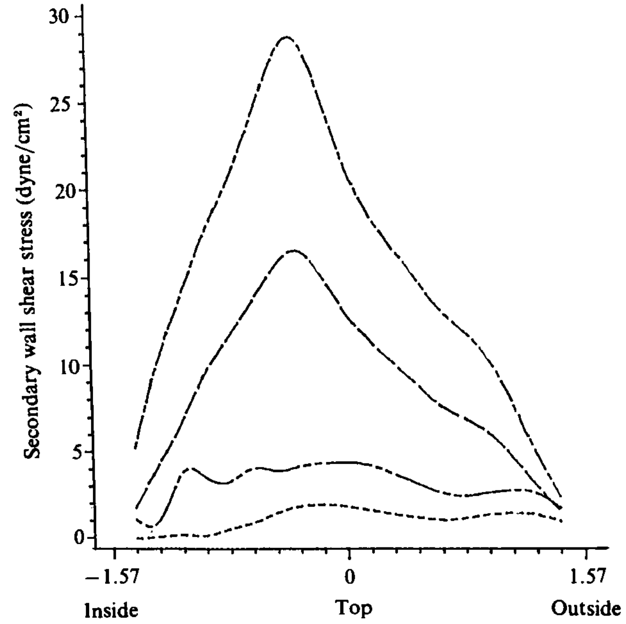

FIGURE 18. Secondary-shear-stress distributions for Exp. IV.
---, $t = 2.15$; –––, 3.52; ––-, 3.83; –––, 6.28.

axial and secondary flows which are pulsatile (figures 12, 13 and 16), but the secondary flow is more complex than suggested by Smith's Case X. The simulations show an outward motion along the centreline during certain intervals of the flow cycle (figure 16*a*, *d*), but during other intervals (figure 16*b*, *c*) the centreline secondary flow changes direction at several locations, reflecting the multiplicity of core vortices. The multiple-core vortices and embedded vortices which distinguish Exp. IV have not been discussed by Smith for Case X. It must, of course, be remembered that Smith's analysis is for a one-harmonic flow, while physiological pulsatile flows are inherently multi-harmonic. Because of the nonlinear nature of curved-tube-flow problems, a superposition principle does not generally apply, and harmonic interactions may lead to new flow structures.

4. Concluding remarks

The numerical solutions for physiological pulsatile flows characteristic of the aortic arch presented in this paper reveal a wide variety of interesting flow phenomena including: (1) complex secondary flows with up to seven vortices in a half-tube; (2) cascaded vortex structures with vortices embedded within vortices; (3) strong secondary flows with associated wall shear stress nearly as large as the axial component; (4) reversal of axial-flow direction at the inside wall; (5) peak axial wall shear stress appearing at the inside wall, whereas it appears on the outside wall in steady flow; (6) highest r.m.s. wall shear stress at the inside wall; and (7) oscillatory impedance which is accurately described by straight-tube theory.

The present work is also perhaps relevant to our understanding of the role of fluid mechanics in atherogenesis. Although the aortic arch is not one of the most prominent sites in the arterial system for severe atherosclerosis (Nerem & Cornhill 1980), it is affected by the disease and most severely on the inner curvature (Texon 1980; Rodkiewicz 1975). The inner curvature would normally be thought a low-wall-shear-stress region on the basis of fully-developed-steady-flow considerations, and indeed we have seen that the (time) mean wall shear stress is lowest in this region. However, the instantaneous wall shear stress and r.m.s. wall shear stress may be highest on the inner curvature. Thus the inner curvature is a site of both low and high wall shear stress relative to the outer curvature. In order to decide whether the mean shear stress or the peak or r.m.s. shear stress is most likely to be influential in the distribution of atheroma, it is necessary to have some appreciation of timescales associated with atherogenic mechanisms which are influenced by wall shear stress. If such mechanisms are slow (time constant much greater than ~ 1 s), such as diffusive mass transport within the artery wall, then the peak and r.m.s. components will be greatly attenuated, and only the mean component will be influential. On the other hand, if such mechanisms are fast (time constant less than ~ 1 s), the peak and/or r.m.s. components may come into play. The peak and/or r.m.s. components may also be important if a threshold mechanism, which 'turns on' only when wall shear stress exceeds a certain minimum value, is operative. Unfortunately, the shear-dependent mechanisms are not well understood at present, and the question remains open.

This work was supported in part by NSF Grant No. MEA 80-10878 and NIH Grant No. HL26824.

REFERENCES

Austin, L. R. & Seader, J. D. 1973 *AIChE J.* **19**, 85.

Berger, S. A., Talbot, L. & Yao, L.-S. 1983 *Ann. Rev. Fluid Mech.* **15**, 461.

Bertelsen, A. F. 1974 An investigation of the oscillating viscous flow in a curved pipe with special emphasis on low Reynolds number secondary streaming effects. *Rep. No. 67, Dept of Physics, University of Bergen, Norway.*

Blennerhassett, P. 1976 Secondary motion and diffusion in unsteady flow in a curved pipe. Ph.D. thesis. Imperial College, London.

Brech, R. & Bellhouse, B. J. 1973 *Cardiovasc. Res.* **7**, 593.

Caro, C. G., Fitz-Gerald, J. M. & Schroter, R. C. 1971 *Proc. R. Soc. Lond.* B **177**, 109.

Chandran, K. B., Swanson, W. M., Ghista, D. N. & Vayo, H. W. 1974 *Ann. Biomed. Engng* **2**, 392.

Chandran, K. B., Hosey, R. R., Ghista, D. N. & Vayo, V. W. 1979 *J. Biomech. Engng* **101**, 114.

Chandran, K. B. & Yearwood, T. L. 1981 *J. Fluid Mech.* **111**, 59.

Dean, W. R. 1927 *Phil. Mag.* **4**, 208.

Fry, D. L. 1968 *Circ. Res.* **22**, 165.

Fry, D. L. 1969 *Circ. Res.* **24**, 93.

Kang, S. G. & Tarbell, J. M. 1983 *J. Biomech. Engng* **105**, 275.

Lin, J. Y. & Tarbell, J. M. 1980 *J. Fluid Mech.* **100**, 623.

Lyne, W. H. 1970 *J. Fluid Mech.* **45**, 13.

Naumann, A. & Schmid-Schonbein, H. 1983 In *Fluid Dynamics as a Localizing Factor for Atherosclerosis* (ed. G. Schettler). Springer.

Nerem, R. M. & Cornhill, J. F. 1980 *J. Biomech. Engng* **102**, 181.

Nerem, R. M. 1981 In *Structure and Function of the Circulation Vol. 2* (ed. Schwartz). Plenum.

Patankar, S. V., Pratap, V. S. & Spalding, D. B. 1974 *J. Fluid Mech.* **62**, 539.

Pedley, T. J. 1980 *The Fluid Mechanics of Large Blood Vessels.* Cambridge University Press.

Rabadi, N. J., Simon, H. A. & Chow, J. C. F. 1980 *Numer. Heat Transfer* **3**, 225.

Rodkiewicz, C. M. 1975 *J. Biomech. Engng* **8**, 149.

Simon, H. A., Chang, M. H. & Chow, J. C. F. 1977 *J. Heat Transfer* **99**, 590.

Singh, M. P., Singha, P. C. & Agarawal, M. 1978 *J. Fluid Mech.* **87**, 97.

Smith, F. T. 1975 *J. Fluid Mech.* **71**, 15.

Tabot, L. & Gong, K. O. 1983 *J. Fluid Mech.* **127**, 1.

Tarbell, J. M. & Samuels, M. R. 1973 *Chem. Engng J.* **5**, 117.

Texon, M. 1980 *Hemodynamic Basis of Atherosclerosis.* Hemisphere.

Womersley, J. R. 1955 *Phil. Mag.* **46** (7), 199.

Yearwood, T. L. & Chandran, K. B. 1984 *J. Biomech.* **15**, 683.

Zalosh, R. G. & Nelson, W. G. 1973 *J. Fluid Mech.* **59**, 693.